2020

Design and optimization of a water jet-based biomimetic antifouling model for marine structures

Guijie Liu

Weixiong Jiang

Zichao Yuan

Yingchun Xie

Xiaojie Tian

See next page for additional authors

Design and optimization of a water jet-based biomimetic antifouling model for marine structures

Abstract

© 2020 Author(s). Marine structures, such as ship hulls and offshore platforms, are basic elements in marine engineering. Due to the harsh ocean environment, marine structures are prone to adhesion and corrosion by marine biofouling. The biomimetic antifouling technology has been recognized as the most promising solution to marine biofouling, while there is still a long way to go to take this technology outside of research laboratories. In order to develop practical biomimetic antifouling techniques, this work presents a new water jet-based biomimetic antifouling model for marine structures to prevent the enrichment of biofouling. First, a semi-empirical formula is proposed based on the Schlichting self-similar solution to determine the effective width of the water jet. Then, a numerical simulation model is established to investigate the effects of the jet parameters (such as the jet aperture, jet velocity, and jet hole spacing) on the water jet distribution. Subsequently, visualization experiments are carried out to compare and validate the numerical simulation results. Finally, the simulation data are used to train a genetic neural network to predict the effective jet coverage ratio. The optimal parameters of the antifouling model are obtained corresponding to the largest effective jet coverage ratio. The findings of this study deliver a practical biomimetic antifouling technique for marine structures.

Disciplines

Engineering | Science and Technology Studies

Publication Details

Liu, G., Jiang, W., Yuan, Z., Xie, Y., Tian, X., Leng, D., Incecik, A. & Li, Z. (2020). Design and optimization of a water jet-based biomimetic antifouling model for marine structures. Physics of Fluids, 32 (9),

Authors

Guijie Liu, Weixiong Jiang, Zichao Yuan, Yingchun Xie, Xiaojie Tian, Dingxin Leng, Atilla Incecik, and Zhixiong Li

Physics of Fluids

Design and optimization of a water jet-based biomimetic antifouling model for marine structures

Cite as: Phys. Fluids **32**, 097101 (2020); https://doi.org/10.1063/5.0020098
Submitted: 27 June 2020 . Accepted: 12 August 2020 . Published Online: 01 September 2020

Guijie Liu (刘贵杰), Weixiong Jiang (江伟雄), Zichao Yuan (原子超), Yingchun Xie (谢迎春), Xiaojie Tian (田晓洁), Dingxin Leng (冷鼎鑫), Atilla Incecik, and Zhixiong Li (李志雄)

Physics of Fluids ARTICLE scitation.org/journal/phf

Design and optimization of a water jet-based biomimetic antifouling model for marine structures

Cite as: Phys. Fluids 32, 097101 (2020); doi: 10.1063/5.0020098
Submitted: 27 June 2020 • Accepted: 12 August 2020 •
Published Online: 1 September 2020

Guijie Liu (刘贵杰),[1,a)] Weixiong Jiang (江伟雄),[1] Zichao Yuan (原子超),[1] Yingchun Xie (谢迎春),[1] Xiaojie Tian (田晓洁),[1] Dingxin Leng (冷鼎鑫),[1] Atilla Incecik,[2] and Zhixiong Li (李志雄)[3,a)]

AFFILIATIONS

[1] Department of Mechanical and Electrical Engineering & Key Laboratory of Ocean Engineering of Shandong Province, Ocean University of China, Qingdao 266100, China

[2] Department of Naval Architecture, Ocean and Marine Engineering, University of Strathclyde, Glasgow, Scotland G1 1XQ, United Kingdom

[3] School of Mechanical, Materials, Mechatronic and Biomedical Engineering, University of Wollongong, Wollongong, NSW 2522, Australia

[a)] **Authors to whom correspondence should be addressed:** liuguijie@ouc.edu.cn and zhixiong.li@ieee.org

ABSTRACT

Marine structures, such as ship hulls and offshore platforms, are basic elements in marine engineering. Due to the harsh ocean environment, marine structures are prone to adhesion and corrosion by marine biofouling. The biomimetic antifouling technology has been recognized as the most promising solution to marine biofouling, while there is still a long way to go to take this technology outside of research laboratories. In order to develop practical biomimetic antifouling techniques, this work presents a new water jet-based biomimetic antifouling model for marine structures to prevent the enrichment of biofouling. First, a semi-empirical formula is proposed based on the Schlichting self-similar solution to determine the effective width of the water jet. Then, a numerical simulation model is established to investigate the effects of the jet parameters (such as the jet aperture, jet velocity, and jet hole spacing) on the water jet distribution. Subsequently, visualization experiments are carried out to compare and validate the numerical simulation results. Finally, the simulation data are used to train a genetic neural network to predict the effective jet coverage ratio. The optimal parameters of the antifouling model are obtained corresponding to the largest effective jet coverage ratio. The findings of this study deliver a practical biomimetic antifouling technique for marine structures.

I. INTRODUCTION

Various marine organisms, such as marine animals, plants, and microorganisms, are likely to attach to the surface of marine structures in the ocean environment.[1–3] The marine biological enrichment is called marine biofouling, which increases navigational resistance and fuel consumption and also causes marine structure damage and life loss.[4–6]

Nowadays, a great number of antifouling techniques have been proposed to resolve the issue of marine biofouling, and it can be categorized into physical antifouling and chemical antifouling methods. The chemical antifouling mainly employs antifouling coating techniques and electrochemical techniques. The first one paints a coating layer on the marine structure surfaces, for example, the organotin antifouling coating, which can release biocides to destroy the organisms and decrease the fouling behavior. The second one usually electrolyzes the copper at an anode to release cupric ions, which inhibits bacterial adhesion. However, these chemicals exert toxic effects on non-target organisms and pollute the marine environment, and they also pose a potential threat to human health

for long-time utilization. Consequently, the antifouling coating and electrochemical techniques have been seriously restricted by the International Maritime Organization (IMO) in the late 1980s.[7]

In contrast, the physical antifouling is very environment friendly but inefficient to eliminate the marine biofouling. For example, an autonomous underwater vehicle (AUV) is often utilized to remove the ship biofouling organisms; however, the cleaning procedure is time-consuming and the ship hull surface is vulnerable to damage by the AUV. An alternative method is the ultrasonic technique.[2] The acoustic wave generated by the ultrasonic device is able to effectively prevent bacterial adhesion, and the larvae and spores on the structure surfaces can be destroyed to inhibit biofilm formation.[8] It should emphasize that the ultrasonic wave endangers non-target halobios; for example, dolphin's sonar system would lose the navigation and positioning function due to ultrasonic interference.[9] As a result, the development of efficiently and environment-friendly compatible alternatives is crucial.

Recently, Liu *et al.*[10] proposed a novel biomimetic antifouling method based on the water jet. This method is inspired by the antifouling mechanism of mucus secreted by kelp epidermis and the outward water jet from shark gills, which form a stable and dynamic antifouling layer on its surface to prevent fouling organisms. Similarly, a water jet layer was established as such a kind of dynamic antifouling layer to prevent the attachment of marine organisms.[10] In our previous work, we conducted numerical simulation as well as the experimental test to evaluate the performance of the proposed antifouling method. The analysis result demonstrated that the water jet-based antifouling does not produce any toxic substances to pollute the marine environment. However, this research did not investigate the optimization of the water jet-based antifouling model, which may hinder its industrial applications.

Abundant theoretical modeling and analysis on different fluid-jet problems has been conducted in the past decades.[11] It provides the foundation for studying the relationship between the jet parameters and the jet distribution. For example, Deguchi *et al.*[12] summarized the Schlichting theory to study the velocity distribution of a plane laminar jet and a circular laminar jet. The theoretical foundation has been established in this work for two-dimensional (2D) laminar jets. However, the Schlichting solution has some drawbacks in terms of the calculation accuracy. The jet field characteristics cannot be precisely described due to that it is a semi-empirical formula. Jermyn *et al.*[13] utilized the mixing length theory to analyze a free turbulent flow and produced the theoretical foundation for 2D turbulent jets. However, according to Prandtl's extensive experimentation, it was found that the viscosity vortex coefficient was not consistent with the experimental results at the point of maximum velocity. Hence, the mixing length theory cannot be used at this point. Furthermore, Hong *et al.*[14] investigated the influence of the geometric parameters of a jet actuator on the jet distribution. The theoretical analysis results showed that the maximum jet velocity is proportional to the pore aperture when the actuation amplitude is a constant. For a consistent jet water volume, there is an optimal jet pore aperture where the maximum jet velocity can be achieved. However, the contradictory results pertain to the impact of the aspect ratio of the rectangular jets on the velocity decay rate in the past decades, and the nonlinear control equation of the jet problem makes it difficult to obtain an accurate analytical solution by theoretical analysis.

Fortunately, a numerical technique can remedy the shortcoming of theoretical analysis, and a numerical solution can be calculated to meet the engineering needs. Meanwhile, with the advent of computer science and the development of efficient computational prowess, it is feasible to analyze the distribution of the water jet in a flow field by the numerical simulation technology. Guha *et al.*[15] simulated the jet diffusion, pressure attenuation, and pressure distribution in a flow field and identified that the simulation results were consistent with the experimental results. The numerical simulation can effectively analyze the jet distribution in the flow field. Wang *et al.*[16] numerically calculated the dynamics of impacting rocks by the particle water jet. The result showed that the numerical simulation method can effectively analyze the rock breaking process under the particle water jet. Lee and Goldstein[17] researched the influence of the fluid properties and the jet geometric parameters on the jet distribution in a flow field by numerical simulation. Compared with the experimental data, the numerical simulation can precisely describe the jet characteristics. Junkar *et al.*[18] assessed the impact of the angle and velocity of jet abrasive particles on the processing of stainless steel. The finite element simulation data agreed well with the experimental results. All in all, the existing excellent research findings have proven that numerical simulation is an effective tool to analyze water jet characteristics by solving the fluid dynamics computation problems in complex situations. However, to our best knowledge, very little work has been found to address antifouling using the water jet-based technology. Liu *et al.*[10] pioneered the research on water jet-based biomimetic antifouling and found that the jet flow can form a dynamic antifouling layer to restrain marine biofouling, but optimizing the model parameters of the new biomimetic antifouling remains a challenge.

In order to address the aforementioned issue, the present work aims to optimize parameters of a new water jet-based biomimetic antifouling model. Numerical simulations were carried out to analyze the jet distribution of the model, and the experimental tests were performed to validate the simulation results. A comparison between simulations and experiments confirmed the designed water jet-based biomimetic antifouling model. Hence, the simulation data were used to predict the effective jet coverage ratio by a genetic neural network (GNN) in order to optimize the model parameters. The optimization result proved the feasibility of the proposed method.

The implementation of this work is organized as follows. In Sec. II, the semi-empirical formula of the jet effective width is deduced. The impact of the jet aperture and the jet velocity on the jet effective width is discussed. In Sec. III, the effect of the jet aperture, the jet hole spacing, and the jet velocity on the effective jet coverage rate is analyzed by numerical simulation. In Sec. IV, the jet visualization experiment is conducted to compare the simulation results. Section V predicts the effective jet coverage ratio using the GNN to determine the optimal jet antifouling model. Section VI summarizes the main conclusions.

II. THEORETICAL ANALYSIS

Figure 1 shows an overview of the proposed research in this study, which consists of three parts: the first one is the theoretical

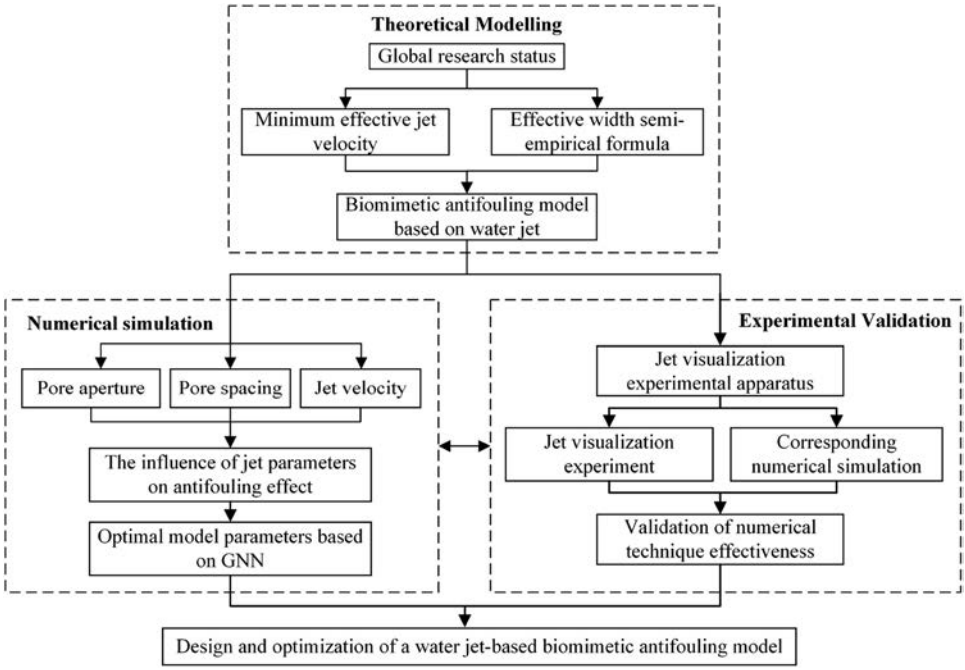

FIG. 1. Overview of the proposed research.

modeling, the second one is the numerical simulation, and the third is the experimental validation.

In the theoretical modeling, the minimum effective jet velocity is first analyzed, and the effective width semi-empirical formula is then established. Hence, a biomimetic antifouling model with a water jet is developed in this part.

Then, numerical simulation is carried out to investigate the effect of different jet parameters on the performance of the antifouling model. Based on the investigation results, the optimal jet parameters are determined in this part.

Finally, in the experimental validation, the jet visualization is compared with the simulation results.

A. Calculation of minimum effective jet velocity

In the ocean environment, there are a lot of marine organisms (such as diatom, barnacle, and oyster), which will cause marine biological enrichment. In this paper, diatom is selected as antifouling objects because it can adhere to the marine structure surface at the very beginning of fouling formation. The diatom was assumed as a cylinder with an outer diameter $D_e = 4\ \mu$m and a length $L = 15\ \mu$m. The cytoplasm density of the diatoms was $\rho_{protoplasma} = 1.046 \times 10^3$ kg/m^3–1.076×10^3 kg/m^3. The thickness of the silicon wall was $t = 100$ nm and its density ρ_s was the same as the silica ($\rho_{silica} = 2.2 \times 10^3$ kg/m^3). The acceleration of gravity $g = 9.8$ g/cm^2. So the volumes of the diatom cytoplasm and silica walls were calculated as follows:

$$V_{protoplasma} = \frac{1}{4}\pi D_e{}^2 gL = 1.885 \times 10^{-16}\ \text{m}^3, \quad (1)$$

$$V_{silica} = \frac{1}{4}\pi D_e{}^2 gL - \frac{1}{4}\pi D_n{}^2 g(L - 2t) = 2.065 \times 10^{-17}\ \text{m}^3, \quad (2)$$

where V_{silica} and $V_{protoplasma}$ are the volumes of the silica and cytoplasm. There are mainly three kinds of forces, including the gravity, the buoyancy, and the short-range forces in still water. The diatom gravity and buoyancy can be calculated as

$$F_{buoyancy} = \rho_{sw}\left(V_{protoplasma} + V_{silica}\right)g = 2.100\,912 \times 10^{-12}\ \text{N}, \quad (3)$$

$$G = \rho_{protoplasma} V_{protoplasma} g + \rho_{silica} V_{silica} g = 2.403 \times 10^{-12}\ \text{N}, \quad (4)$$

where G is the gravity of the diatom, and $F_{buoyancy}$ is the diatom buoyancy. The diatom density can be controlled by the bubbles using the photosynthesis, which could be less than or equal to the density of the sea water. So the diatom can float or suspend in the water.[19] Therefore, the present study assumes the sum of diatoms' gravity and buoyancy as 2×10^{-12} N, and the force direction is vertical and upward,

$$F_{sum} = F_{buoyancy} + G \approx 2 \times 10^{-12}\ \text{N}. \quad (5)$$

The minimum effective jet velocity can be calculated according to the relationship between the jet velocity and the pressure as follows:

$$u_{\min} = \sqrt{\frac{F_{sum} + F_{mlc}^{XDLVO}}{\rho A}}, \quad (6)$$

where ρ is the jet density, A is jet pressure area, and F_{mlc}^{XDLVO} is the short-range force on the diatom. Generally, F_{mlc}^{XDLVO} can be neglected because the buoyancy is much higher than the short-range force.[20] Then, the critical jet velocity was obtained as 3.6×10^{-3} m/s. In practice, the effective jet velocity could choose 5×10^{-3} m/s to overcome the buoyancy and the short-range forces in still water.

B. Effective width semi-empirical formula

Semi-empirical theory and similarity hypothesis have been widely applied to different jet flow problems in the past decades. Experimental tests are then used to verify the correctness of the simulation models. One typical theory is the Schlichting self-similar solution. The stress distribution of the circular turbulent jet is deduced through the Schlichting solution based on the assumption of similar velocity distribution on the cross section. Furthermore, combining the Schlichting self-similar solution with the flow function,[21,22] the velocity distribution, which is perpendicular to the jet hole surface, can be expressed as

$$u = \frac{3}{8\pi}\frac{J}{\nu_t x\rho}\frac{1}{\left(1+\frac{1}{4}\eta^2\right)^2}, \tag{7}$$

where $\eta = \sqrt{\frac{3J}{16\pi\rho}}\frac{r}{\nu_t x}$, ν_t is the vortex viscosity coefficient, r denotes the coordinates perpendicular to the jet direction, x denotes the coordinates along the jet direction, and J denotes the momentum flux of the jet. Since the momentum flux of each section of the jet is equal to the momentum flux of the outlet section, it yields

$$J = \int_0^\infty \rho u^2 2\pi r dr = \rho u_0^2 \pi r_0, \tag{8}$$

where μ_0 and r_0 denote the velocity and the radius of the jet exit, respectively. In order to analyze the impact of the jet parameters on the antifouling performance, a semi-empirical formula for the effective jet width is derived based on the Schlichting self-similar solution. Combining Eq. (7) with Eq. (8), one can get the relationship between r and x as follows:

$$r = \sqrt{\frac{1}{\sigma^2}\left(\frac{\sqrt{6}u_0 r_0}{\sqrt{u\nu_t}}x^{\frac{3}{2}} - 4x^2\right)}, \tag{9}$$

where σ is an empirical constant, ν_t is the kinematic viscosity of the fluid, and u is the velocity of the jet at a point in the flow field.

As can be seen in Eq. (9), the semi-empirical formula not only can minimizes the effective jet width using the minimum effective jet velocity[9] but also can reflect the effect of the jet velocity and the jet aperture on the effective jet width. According to Eq. (9), the effective jet width increases with the increase of the jet velocity/jet aperture. This impact law provides theoretical support to the subsequent numerical simulation and experimental analyses.

III. NUMERICAL SIMULATION ANALYSIS

The impact law of the jet aperture and the jet velocity on the effective jet width is preliminarily understood in the semi-empirical formula. In this section, numerical simulations are carried out to quantitatively estimate the relationship between the jet parameters and the effective jet width. The jet distribution is analyzed by the effective jet coverage ratio at the cross section in the flow field. The image processing software Adobe photoshop is utilized to count the total pixel number of the cross section (N_{all}) and the pixel number of the effective jet area (N_{effect}). The effective jet coverage ratio (η_{effect}) can be calculated as follows:

$$\eta_{\text{effect}} = \frac{N_{\text{effect}}}{N_{\text{all}}} \times 100\%. \tag{10}$$

One can note that the larger the jet effective width, the better the effective jet coverage ratio.

A. Finite element model

In a real physical system, the control of the jet problem is generally expressed in nonlinear equations. The complicated geometry and boundary conditions of the computational domains make it difficult to obtain an accurate analytical solution by the theoretical analysis. A numerical solution can be calculated to remedy the shortcoming of the theoretical analysis using the finite element analysis (FEA) and computational fluid dynamics (CFD) techniques.[23–25] In addition, the water jet-based biomimetic antifouling model with different jet velocities, jet apertures, and jet hole spacings can be conveniently established to conduct the numerical simulations.[26] It is time-saving and economic, and is not limited by physical and experimental models.[27] It can easily simulate ideal conditions (such as special jet dimension and extreme jet velocity) that can hardly be achieved in the laboratory to avoid causing damage to experimental facility and threatening life safety. Hence, the FEA and CFD are adopted to establish and analyze the new water jet antifouling model.

The simulation model consists of thousands of basic units. Figure 2 shows one basic unit, where a bidirectional and symmetrical arrangement of four jet holes are employed for the antifouling model. This is because a single- or double-hole model cannot fully consider all interaction directions of the jets. The size of the main flow field of the model is 10 × 10 × 5 mm^3 and the length of the jet hole is 3 mm. Numerical simulations were performed by ANSYS

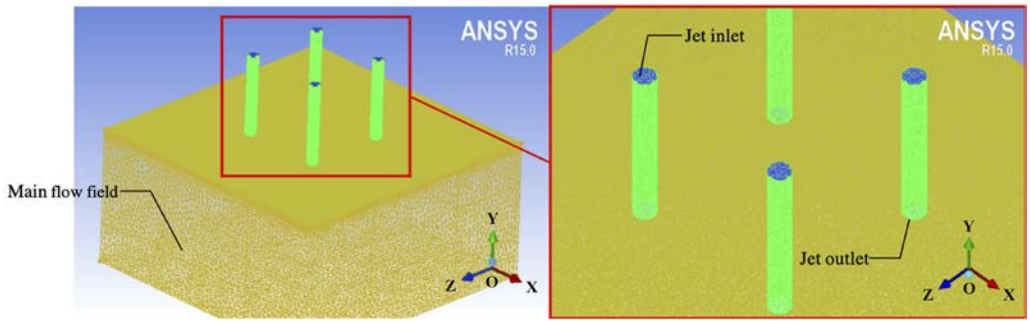

FIG. 2. Meshing result of the four-hole jet antifouling model.

TABLE I. Parameters of the four-hole jet model.

Jet aperture (mm)	Jet hole spacing (mm)	Jet velocity (m/s)
		0.1
	0.75	0.2
0.1	1.5	0.3
0.2	2.25	0.4
0.3	3	0.5
0.4	3.75	0.6
0.5	4.5	0.7
0.6	5.25	0.8
0.7	6	0.9
		1.0

Fluent 15.0. The meshing of the model was processed by ICEM CFD 15.0. The grid generation result after grid quality verification is shown in Fig. 2. In the simulation, the inlet face boundary adopted the velocity inlet; the wall boundary of the jet pore and the upper surface boundary of the flow field were set as a wall; the remaining five faces of the flow field were set as the pressure outlet and the outlet pressure was set to zero. A series of empirical values were selected for the jet aperture, jet hole spacing, and jet velocity. The values of these model parameters are listed in Table I.

Previous research[10] found that the fluid flow in the jet pore is approximately in the laminar state and the fluid in the flow field is in the turbulent state. Because the renormalization group k-epsilon (RNG k-ε) model[28,29] is able to provide an effective viscosity differential formula to deal with low Reynolds fluids, the viscous model chose the RNG k-ε model in this study. Considering the gravity, the jet can be analyzed and observed by steady state analysis. In order to quantitatively inspect the antifouling effect of the simulation model, the jet effective coverage ratio is adopted as the evaluation index.[10] Generally, an antifouling model can be regarded effective if the jet effective coverage ratio reaches 95% or more.

B. Simulation results

1. Effect of the jet aperture

Based on one basic unit, numerical simulation is first conducted to assess the effect of the jet aperture on the effective jet coverage ratio. In the simulation analysis, the jet hole spacing was fixed at 3 mm and the jet velocity was 0.5 m/s. The velocity contours of the antifouling unit were calculated by changing the jet aperture from 0.1 mm to 0.7 mm. Figure 3 portrays the velocity contours, where

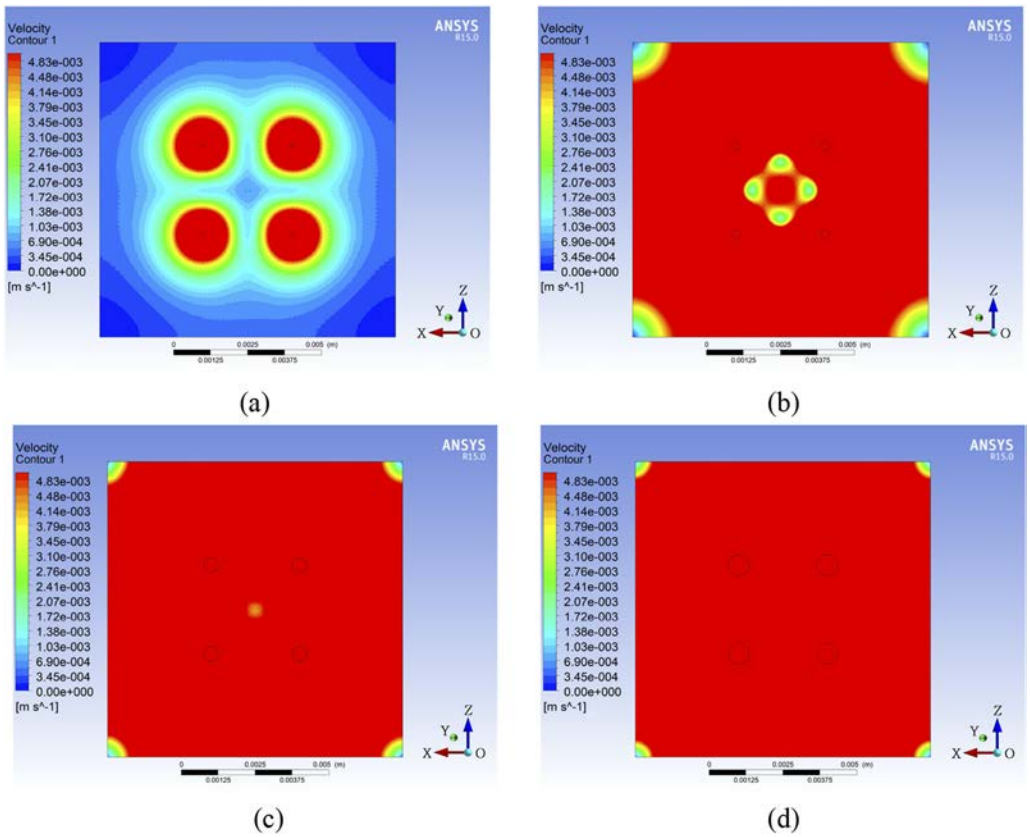

FIG. 3. Velocity contours of an antifouling unit with different jet aperture values. (a) Aperture is 0.1 mm; (b) aperture is 0.3 mm; (c) aperture is 0.5 mm; and (d) aperture is 0.7 mm.

TABLE II. The effective jet coverage ratio at different jet aperture values.

Aperture (mm)	0.1	0.2	0.3	0.4	0.5	0.6	0.7
Effective jet coverage ratio (%)	10.01	76.15	91.36	96.29	97.51	98.03	98.21

the color bar indicates the intensity of the effect of the jet flow on the effective jet coverage ratio. The red area represents the minimum effect area. The red area gradually expands from the vicinity of the jet nozzle with an increase in the jet aperture.

Table II shows the effective jet coverage ratio of the antifouling unit with respect to different jet aperture values. As can be seen in the table, the effective jet coverage ratio increases with an increase in the jet aperture at fixed jet hole spacing and jet velocity values. The effective jet coverage ratio is greater than 95% when the jet aperture is greater than 0.4 mm. Furthermore, the change in the mechanism of the effective jet coverage ratio is discussed using different aperture-spacing and different aperture-velocity values, as shown in Fig. 4.

In Fig. 4(a), the effective jet coverage ratio is calculated using different aperture-spacing values at 0.5 m/s of the jet velocity. When the jet aperture increases, the effective jet coverage ratio increases quickly before the aperture reaches 0.3 mm. Then, the effective jet coverage ratio gradually enters a stable state no matter how the jet aperture increases. In addition, when the jet aperture is larger than 0.3 mm, the effective jet coverage ratio is generally better at 3.0 mm of the jet hole spacing than those at other spacing values.

In Fig. 4(b), the effective jet coverage ratio is calculated using different aperture-velocity values at 3.0 mm of the jet hole spacing. The effective jet coverage ratio basically increases with the jet aperture; however, the jet velocity has a significant impact on the effective jet coverage ratio. Increasing the jet velocity improves the effective jet coverage ratio.

2. Effect of jet hole spacing

Then, numerical simulation is implemented to analyze the effect of the jet hole spacing on the effective jet coverage ratio. In the simulation analysis, the jet aperture was fixed at 0.6 mm and the jet velocity was 0.5 m/s. The velocity contours of the antifouling unit were calculated from 0.75 mm to 6.0 mm of the jet hole spacing. Figure 5 shows the velocity contours. As can be seen, the red area is mainly concentrated near the jet nozzles when the jet hole spacing is small, and gradually disappears in the middle of the nozzles when the jet hole spacing exceeds 3.75 mm.

Table III shows the effective jet coverage ratio at different jet hole spacings. As can be seen in the table, the effective jet coverage ratio first increases and then decreases with an increase in the jet hole spacing at constant jet aperture and jet velocity values. The effective jet coverage ratio meets the requirements of the antifouling effect when the hole spacing is less than 3.75 mm.

The change trends of the effective jet coverage ratio with different spacing-aperture and different spacing-velocity values are shown in Fig. 6. In Fig. 6(a), the effective jet coverage ratio is calculated using different spacing-aperture values at 0.5 m/s of the jet velocity. The ratio basically increases first and then decreases with an increase in the jet hole spacing.

In Fig. 6(b), the effective jet coverage ratio is calculated using different spacing-velocity values at 0.6 mm of the jet aperture. There is no specific change law for the effective jet coverage ratio in the figure; however, when the jet velocity is 1.0 m/s, the ratio is the best at each spacing point.

3. Effect of the jet velocity

Finally, the effect of the jet velocity on the effective jet coverage ratio is discussed. In the simulation analysis, the jet aperture was fixed at 0.6 mm and the jet hole spacing was 4.5 mm. The velocity contours were calculated from 0.1 m/s to 1.0 m/s of the jet velocity. Figure 7 shows the calculation results, where the red area expands

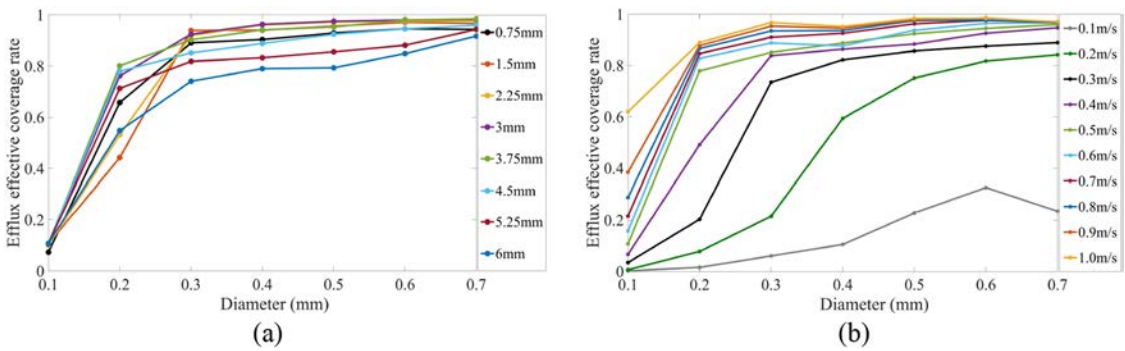

FIG. 4. Change trends of the effective jet coverage ratio. (a) Aperture-spacing curves and (b) aperture-velocity curves.

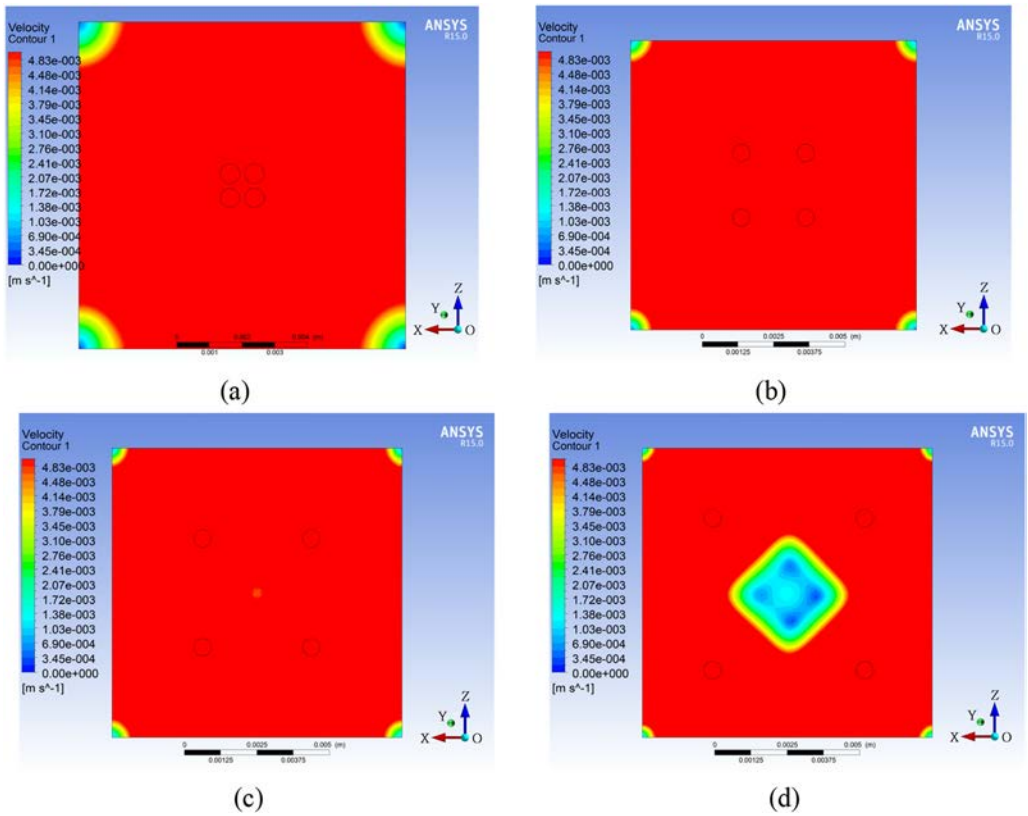

FIG. 5. Velocity contours of an antifouling unit with different jet hole spacings. (a) Hole spacing = 0.75 mm; (b) hole spacing = 2.25 mm; (c) hole spacing = 3.75 mm; and (d) hole spacing = 5.25 mm.

TABLE III. The effective jet coverage ratio at different jet hole spacing values.

Aperture (mm)	0.75	1.5	2.25	3	3.75	4.5	5.25	6
Effective jet coverage ratio (%)	94.54	97.11	97.56	98.03	98.05	94.51	88.12	84.86

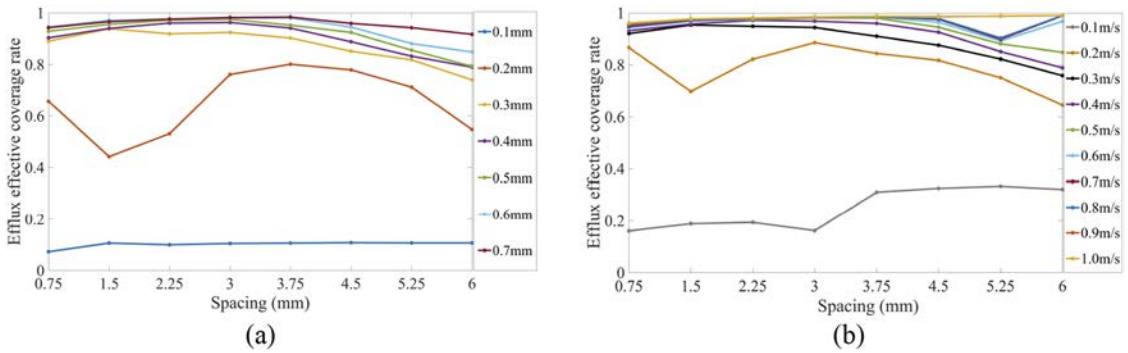

FIG. 6. Change trends of the effective jet coverage ratio. (a) Spacing-aperture curves and (b) spacing-velocity curves.

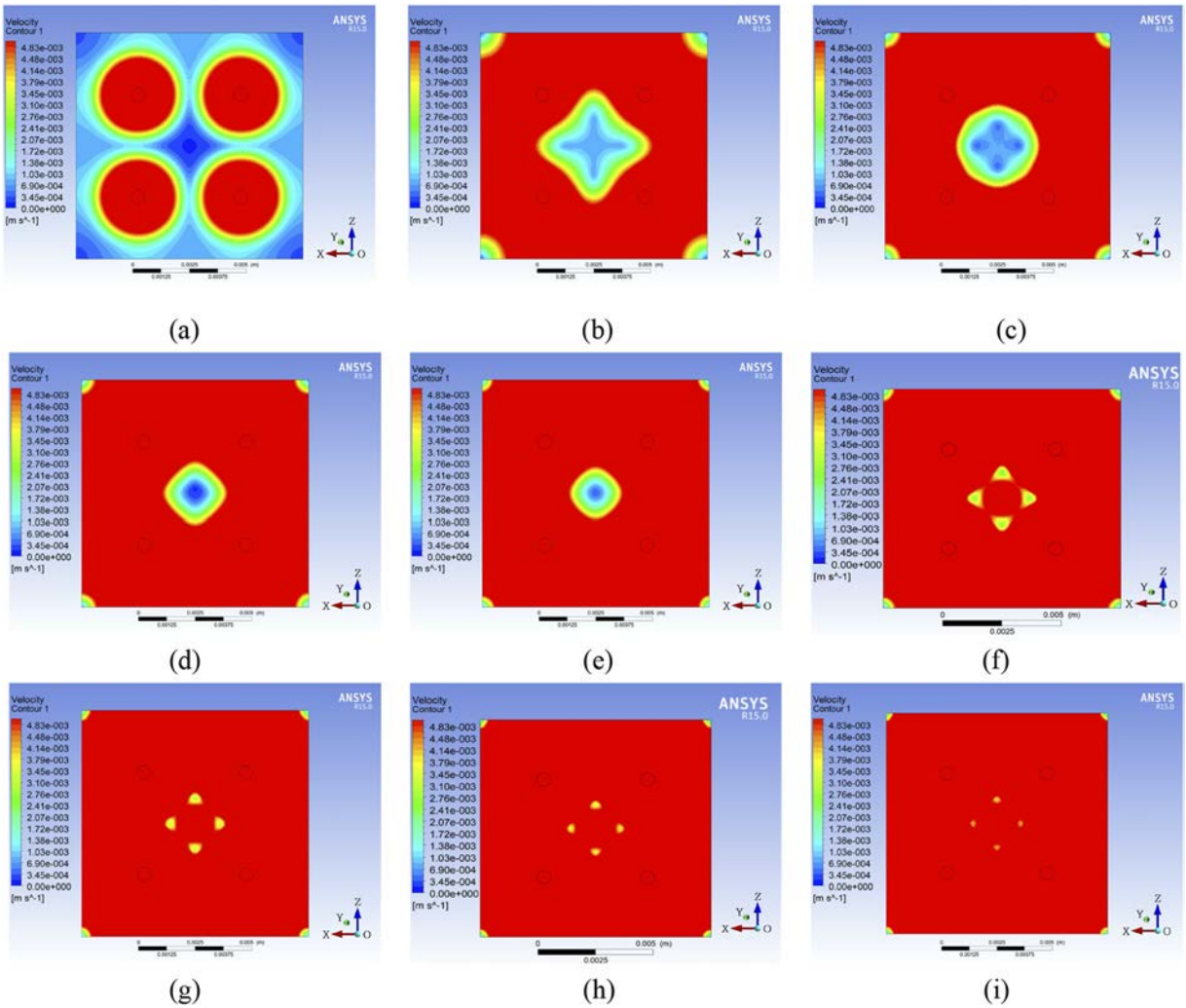

FIG. 7. Velocity contours of different jet velocity. (a) Jet velocity = 0.1 m/s; (b) jet velocity = 0.2 m/s; (c) jet velocity = 0.3 m/s; (d) jet velocity = 0.4 m/s; (e) jet velocity = 0.5 m/s; (f) jet velocity = 0.6 m/s; (g) jet velocity = 0.7 m/s; (h) jet velocity = 0.8 m/s; and (i) jet velocity = 0.9 m/s.

from the vicinity of the jet nozzles to the whole section of the unit when the jet velocity increases.

Table IV gives the effective jet coverage ratio at different jet velocity values. As can be seen in the table, the ratio increases with an increase in the jet velocity. The effective jet coverage ratio is greater than 95% when the jet velocity is greater than 0.6 m/s.

TABLE IV. The effective jet coverage ratio at different jet velocities.

Velocity (m/s)	0.1	0.2	0.3	0.4	0.5
The effective jet coverage ratio (%)	32.61	81.75	87.59	92.62	94.51
Velocity (m/s)	0.6	0.7	0.8	0.9	1.0
The effective jet coverage ratio (%)	96.46	97.61	97.85	98.56	98.44

The change trends of the effective jet coverage ratio with different velocity-aperture and different velocity-spacing values are shown in Fig. 8. In Fig. 8(a), the effective jet coverage ratio is calculated using different velocity-aperture values at 4.5 mm of the jet hole spacing. The ratio increases with an increase in the jet velocity and the jet aperture.

In Fig. 8(b), the effective jet coverage ratio is calculated using different velocity-spacing values at 0.6 mm of the jet aperture. The ratio increases with an increase in the jet velocity, but no specific change law is observed for the jet spacing.

Based on these observations one can note that the effective jet coverage ratio increases with the jet aperture and jet velocity, while the change law is not clear for the jet hole spacing. According to Eq. (5), the effective jet width increases with an increase in the jet velocity/jet aperture. As a result, the simulation results are consistent with the semi-empirical formula.

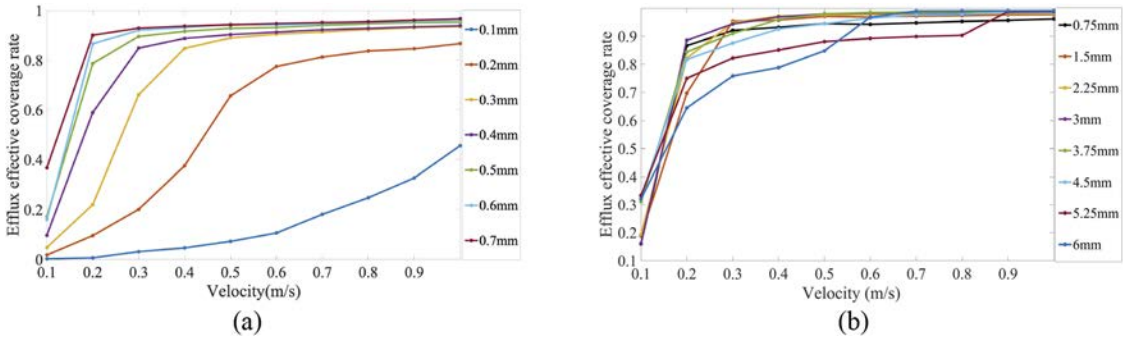

FIG. 8. Change trends of effective jet coverage ratio. (a) Velocity-aperture curves and (b) velocity-spacing curves.

IV. JET VISUALIZATION EXPERIMENT

A. Experimental principle and device design

In order to compare the simulation results, jet visualization experiments have been conducted. The jet visualization experiment device consists of four parts:[30–32] one flow control unit, one jet observation unit, one support unit, and one jet plate fixing unit. The details of the experiment device are shown in Fig. 9. The flow control unit is composed of a height ruler and a water box. The corresponding height of a specific jet velocity can be calculated. The height of the water box can be adjusted according to the jet velocity. The observation unit consists of a depth scale and an observation water tank. In this unit, the jet phenomenon can be observed and the data such as the jet distance can be recorded. The support unit is made of aluminum alloy profiles in order to keep the device stable. The jet plate fixing unit is composed of a barn-type fixing bucket and a jet plate, and the two components are bonded and sealed by hot melt adhesive. A laser cutting machine has been used to manufacture a certain size jet holes in the jet plate.

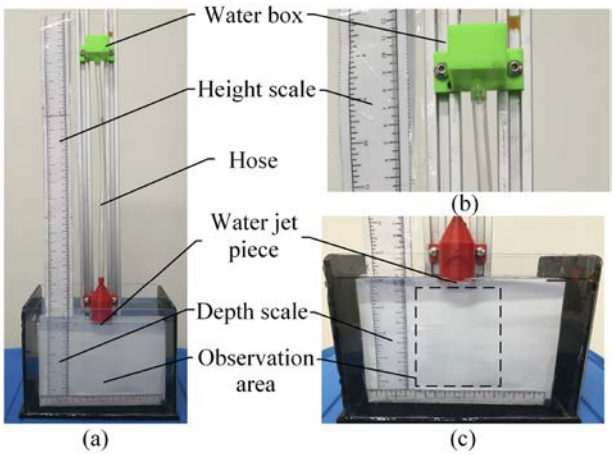

FIG. 9. Jet visualization experimental device. (a) An overview; (b) the flow control unit; and (c) the jet observation unit.

B. Experimental results

The jet distribution at different jet velocities was observed in the jet experiment with 0.4 mm of the jet aperture and 4.5 mm of the jet hole spacing. Four jet holes were arranged symmetrically in the jet plate similar to that in the simulation. The jet distribution was observed at the jet velocities of 0.3 m/s, 0.6 m/s, and 0.9 m/s, respectively. The according heights of the water box were, respectively, 5 mm, 18 mm, and 40 mm. Ink was continuously supplied to the water box to ensure the stable jet velocity. After the jet in the observation area was stabilized, photographs were recorded.

Double-hole jets and multi-hole jets are widely utilized in practical engineering applications. The flow distribution can be divided into a convergence zone and a unite zone in the flow field. There is a boundary point between the convergence zone and the unite zone, which is called the free stagnation point at the end of the convergence zone, as shown in Fig. 10. In the present work, the free stagnation point is used to verify the grid independence and assess the impact of the jet velocity on the jet distribution.[33]

Grid independence was verified in this paper, as shown in Fig. 11, where the distance between the free stagnation point and the jet hole was calculated with different grid resolutions. When the number of mesh increases to ~7×10^6, the distance started to remain stable. In order to select the appropriate grid resolution, the experimental data were compared with the numerical result with three different grid resolutions (i.e., 1.6×10^6, 7×10^6, and 30×10^6 grids) at 0.9 m/s of the jet velocity in terms of the position of the free stagnation point and the jet shape.

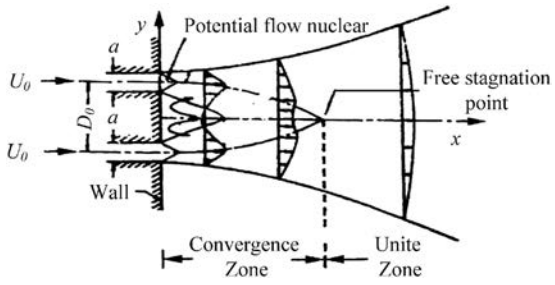

FIG. 10. Schematic diagram of free stagnation points.

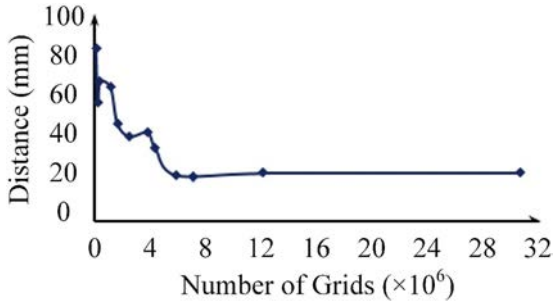

FIG. 11. Grid independence verification.

As can be seen in Figs. 12(b)–12(d), the tails of the jet decrease with an increase in the grid resolution. By doing so, the free stagnation points of the three grid resolutions are 42 mm, 20 mm, and 19 mm, respectively. In Fig. 12(a), the free stagnation point of the experiment under the same condition of the simulation is 18 mm. As a result, the calculation results using 7×10^6 and 30×10^6 grids are close to the experimental measurement. If there is a continuous increase in the grid resolution, the free stagnation point is basically stable around 20 mm. Hence, for a better trade-off between the computation cost and the accuracy, the grid resolution adopted 7×10^6 grids in the following analysis.

The experimental and simulation results are compared at the jet velocities of 0.3 m/s and 0.6 m/s, as shown in Fig. 13. As shown in Fig. 13(a), the free stagnation point is 97 mm in the experiment, while the simulation result is 102 mm at 0.3 m/s of the jet velocity. In Fig. 13(b) the free stagnation points in the experiment and simulation are, respectively, 35 mm and 40 mm at 0.6 m/s of the jet velocity, while in Figs. 12(a) and 12(c), they are 17 mm and 20 mm at 0.9 m/s of the jet velocity. As can be seen, the distance between the free stagnation point and the nozzle is extremely close between the experimental and the simulation results. The jet distribution in the flow field obtained by the numerical simulations is consistent with that in the experimental tests. Thus, the developed numerical model is feasible and effective to analyze the change law of the jet distribution with different model parameters.

V. OPTIMIZATION OF MODEL PARAMETERS

Based on the theoretical and numerical analysis, one can note that effective jet coverage rate of the proposed antifouling model is influenced by the jet velocity, jet aperture, and jet hole spacing. The coverage rate has a positive relationship with the jet velocity and jet aperture; however, the effect of the jet hole spacing on the coverage rate is not clear. As a result, it must optimize these three parameters to produce the best performance of the antifouling model.

In order to address the optimization problem of the model parameters, this section proposes a GNN-based method that is able to optimize the antifouling model performance for any given two jet parameters. In the optimization process, the GNN is first trained by the simulation data acquired under various operating conditions of the antifouling model. Then, given arbitrary two jet parameters, the GNN predicts the optimal third jet parameter to generate the best effective jet coverage rate under this given condition. As a result, the proposed method can obtain the optimal jet parameters for any operating condition of the antifouling model.

Figure 14 gives the training process of the proposed GNN method. A five-layer artificial neural network is used, i.e., a $3 \times 6 \times 4 \times 6 \times 1$ basic structure. The inputs of the network are the three jet parameters, while the output is the effective jet coverage rate. In order to learn the nonlinear relationship between the input and the output data, the genetic algorithm (GA)[34–36] is adopted to train and find the global optimal weight and bias coefficients between any two network layers. After training, a map between the jet parameters and the coverage rate is established.

In the present study, the numerical model was simulated based on the combination of the three jet parameters in Table I to generate 630 pairs of input–output datasets. Five hundred pairs were randomly selected from the 630 datasets to train the GNN. Thirty pairs were utilized as a verification group to inspect whether the

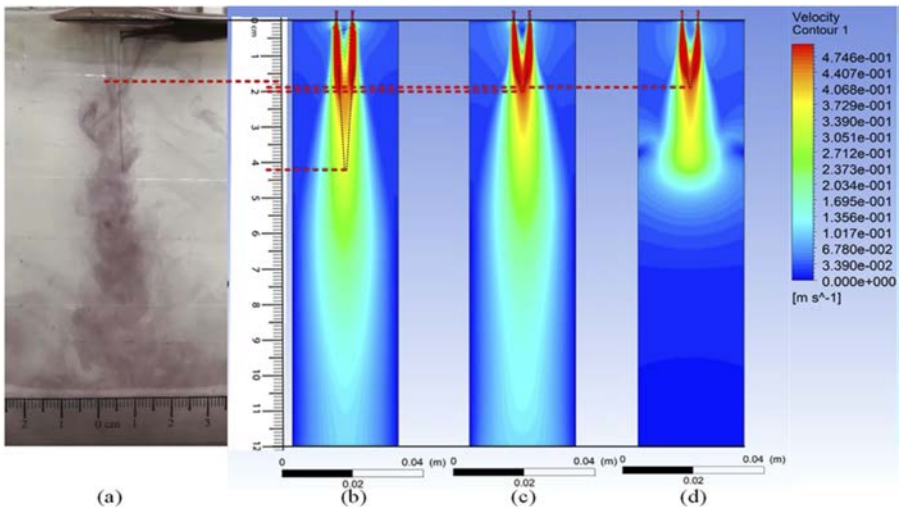

FIG. 12. Comparison results. (a) Experimental results; (b) 1.6×10^6 grids; (c) 7×10^6 grids; and (d) 30×10^6 grids.

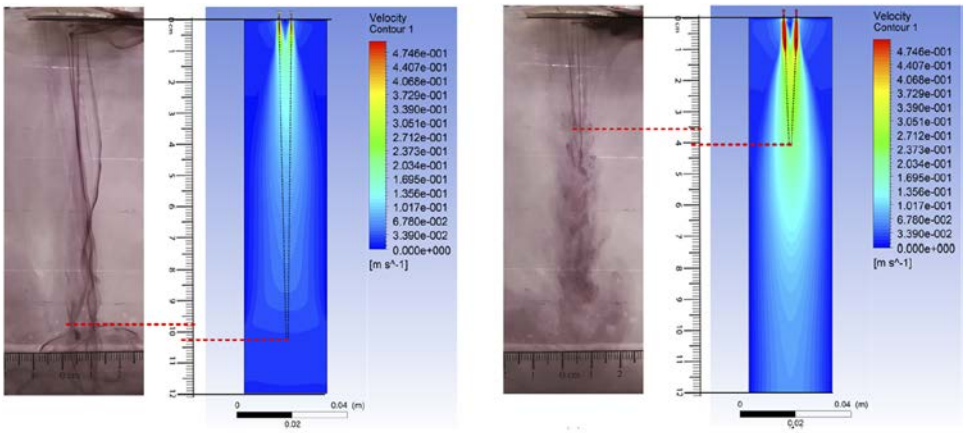

FIG. 13. Comparison between the experimental and the numerical simulation results. (a) Velocity = 0.3 m/s and (b) velocity = 0.6 m/s.

GNN model was overfitted, and the remaining 100 pairs were used as a test group to evaluate the generalization ability of the well-trained GNN model.

In the training process, the GA iteration number was 10, the population size was 20, and the crossover probability and the mutation probability were, respectively, 30% and 10%.

The neuron threshold and activation function were introduced to transform the input signal from negative infinity to positive infinity into an output between 0 and 1 in order to avoid the influence of the magnitude difference between the input data on the prediction accuracy of the model,

$$y_i = f\left(\sum_{i=1}^{n} w_i x_i - \theta_i\right), \tag{11}$$

where f is the activation function, w_i is the weight, x_i is the input, θ_i is the neuron threshold, and y_i is the output after transformation.

Mean square error and determination coefficient were introduced to describe the accuracy of the model training as follows:

$$MSE = E(\hat{y}_i - y_i)^2 (i = 1, 2, 3 \ldots, l), \tag{12}$$

$$R^2 = \frac{\left(l\sum_{i=1}^{l} \hat{y}_i y_i - \sum_{i=1}^{l} \hat{y}_i \sum_{i=1}^{l} \hat{y}_i\right)^2}{\left[l\sum_{i=1}^{l} \hat{y}_i^{\,2} - \left(\sum_{i=1}^{l} \hat{y}_i\right)^2\right]\left[l\sum_{i=1}^{l} \hat{y}_i^{\,2} - \left(\sum_{i=1}^{l} \hat{y}_i\right)^2\right]}, \tag{13}$$

where $\hat{y}_i$ is the effective coverage of the jet obtained by numerical simulation, y_i is the predicted effective coverage of the jet, and l is the number of sample groups.

The analysis results of the GNN model on the training datasets, verification datasets, and test datasets are shown in Fig. 15. As can be seen, the determination coefficients of these datasets are 98.519%, 98.604%, and 98.454%, respectively, and the overall accuracy of the GNN model reaches 98.511%. As a result, the trained GNN model has established an accurate map to connect the jet parameters and the effective jet coverage rate.

In order to further analyze the GNN model, the test datasets were repeatedly predicted for 50 times and the median value of the

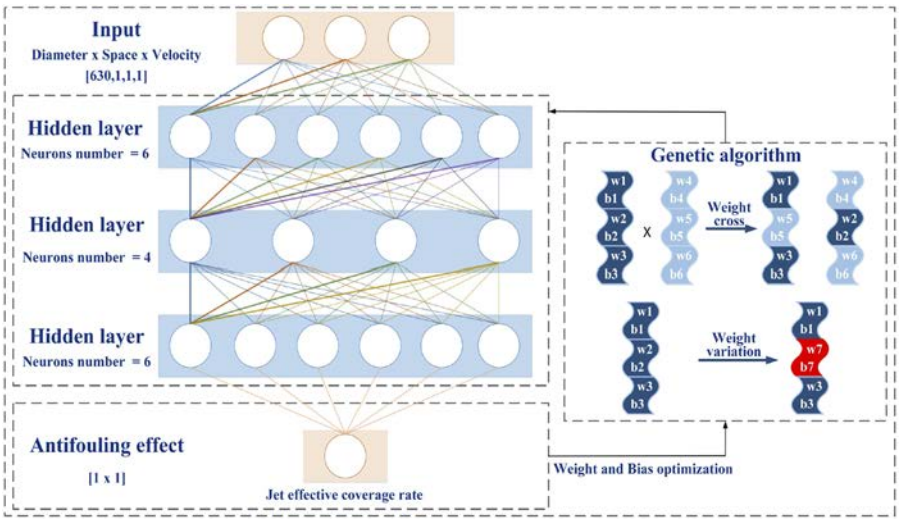

FIG. 14. Flow chart of the prediction of efflux effective coverage by the genetic neural network.

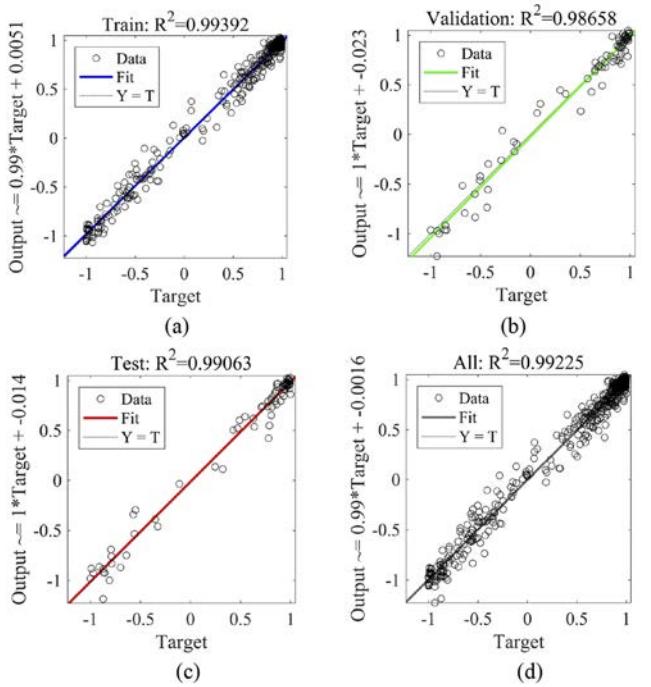

FIG. 15. Accuracy of the training set, verification set, and test set of the GNN model. (a) Training set; (b) validation set; (c) test set; and (d) overall.

prediction results was used to eliminate the stochastic error of the GNN model. Figure 16 manifests the prediction results. As can be seen, when input the three jet parameters into the well-trained GNN model, the effective coverage rate can be predicted at an accuracy of 98.373%. Hence, it is possible to use the GNN model to optimize the model parameters based on the predicted coverage rate.

In real-world applications, we can design the two jet parameters at first according to the installation space, operating requirements, and other specifications. Then, search the third jet parameter using the GNN model. Figure 17 depicts three examples to illustrate the

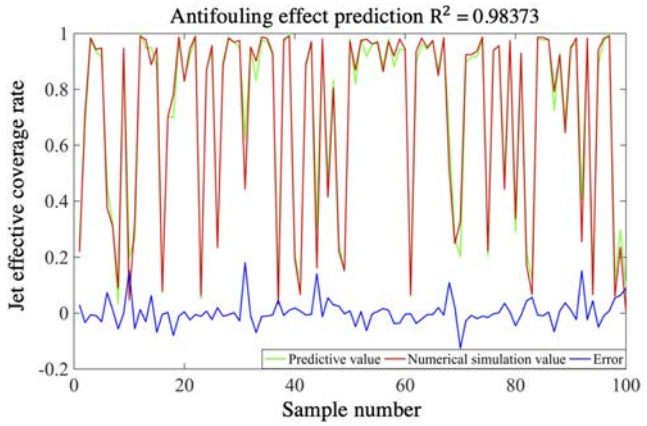

FIG. 16. Comparison of the predicted value with the simulated value.

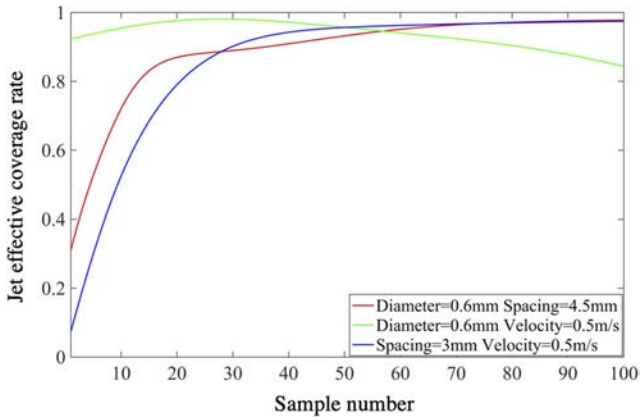

FIG. 17. Optimization of the antifouling model.

parameter optimization. In the first one, as far as we know, the jet aperture is 0.6 mm and the jet hole spacing is 4.5 mm, a curve of the effective jet coverage rate of the antifouling model can be drawn by the GNN under this operating condition. The best coverage rate can be observed and the corresponding jet velocity is 1.0 m/s. Thus, the optimal model parameters can be determined in this example. The same for the other two examples.

In case that only one jet parameter is known, the proposed GNN optimization is also applicable. One can first choose another suitable jet parameter according to the specific working environment, and then use the GNN to search the third one. As a result, the proposed method is effective and powerful for the optimization of the antifouling model.

VI. CONCLUSIONS

In this study, an innovative water jet biomimetic antifouling method based on the mechanism of mucus secreted by kelp epidermis and the outward water jet from shark gills is proposed. A stable and dynamic antifouling layer on the marine structure surface can be formed by means of outward jets. Marine biofouling attachment can be effectively prevented at the very beginning of fouling formation by this method, which does not produce any toxic substances to pollute the marine environment. Subsequently, the novel water jet-based biomimetic antifouling method can compensate for the drawbacks of chemical and physical antifouling methods in terms of environmental pollution and antifouling efficiency. The main conclusions are summarized as follows:

(1) A semi-empirical formula of the jet effective width is deduced based on the Schlichting solution. The formula reveals the impact of the jet aperture and the jet velocity on the jet effective width. The jet effective width increases with the increment in the jet aperture and the jet velocity. So, this formula is beneficial in understanding the physical mechanisms of the water jet in the flow field.

(2) Evaluation indicators and methods of jet antifouling effect is proposed. The impact of jet parameters (e.g., the jet aperture, jet velocity, and jet hole spacing) on the jet effective coverage rate is figured out by numerical simulation analysis; and

jet visualization experiments further verify the correctness of simulation analysis.

(3) An accurate map is obtained by the GNN to connect the jet parameters and the effective jet coverage ratio. The optimal parameters of the antifouling model can be determined at the highest effective jet coverage ratio point by this map, which avoids the waste of time and money by blindly selecting antifouling models.

The influence of the jet parameters on the antifouling performance is further explored using the experimental tests in the future, and the actual antifouling performance of the optimal antifouling model is also studied to facilitate its industrial generalization. In addition, there are several issues that need to be addressed before this proposed method is applied to real world applications; these issues include the selection and processing of the antifouling model material and the jet water resource. In our next study, we use flexible composite materials thanks to their low density, excellent mechanical properties, and corrosion resistance ability;[37,38] for example, we select ethylene tetrafluoroethylene (ETFE) as the antifouling model material. The laser technique[39,40] is employed to produce a porous jet layer. Seawater is used as the jet water resource, and the jet power can be provided by the navigation negative pressure or pumps to form a stable and dynamic antifouling layer on the marine structure surface.[41]

ACKNOWLEDGMENTS

The author(s) disclosed the receipt of the following financial support for the research, authorship, and/or publication of this article: This work was supported by the Shandong Provincial Key Scientific Creation Foundation, China (Grant No. 2019JZZY010820), Shandong Provincial Natural Science Foundation, China (Grant No. ZR201709240210), Applied Fundamental Research Project of Qingdao, China (Grant No. 2019-9-1-14-jch), and Australia Research Council (Grant No. DE190100931).

DATA AVAILABILITY

The data that support the findings of this study are available from the corresponding author upon reasonable request.

REFERENCES

[1] H.-C. Flemming, "Biofouling in water systems - cases, causes and countermeasures," Appl. Microbiol. Biotechnol. **59**(6), 629–640 (2002).
[2] D. M. Yebra, S. Kiil, and K. Dam-Johansen, "Antifouling technology-past, present and future steps towards efficient and environmentally friendly antifouling coatings," Prog. Org. Coat. **50**(2), 75–104 (2004).
[3] F. Liu, S. Gao, Z. Tian, and D. Liu, "A new time-frequency analysis method based on single mode function decomposition for offshore wind turbines," Mar. Struct. **72**, 102782 (2020).
[4] G. J. Liu, Y. F. Sun, B. L. Zhong, Y. C. Xie, A. Incecikb, and Z. X. Li, "Analysis of wind load effect on key components in a jack-up offshore platform," Appl. Ocean Res. **101**, 102263 (2020).
[5] M. S. Selim and M. A. Shenashen, "Progress in biomimetic leverages for marine antifouling by nanocomposite coatings," J. Mater. Chem. B **8**(17), 3701 (2020).
[6] S. Cao, J. Wang, H. Chen, and D. Chen, "Progress of marine biofouling and antifouling technologies," Chin. Sci. Bull. **56**(7), 598–612 (2011).
[7] S. M. Olsen, L. T. Pedersen, M. H. Hermann, S. Kiil, and S. Dam-Johansen, "Enzyme-based solutions for marine antifouling coatings," Adv. Mar. Antifouling Coat. Technol. **13**(6), 623–643 (2009).
[8] K. Thiruppathi, P. Lakshmi, K. Sudarsan, D. Rajapan, and R. Kirubagaran, "A study on the effect of pulsed power ultrasound waves on marine biofouling," Indian J. Geo-Mar. Sci. **43**(11), 2169–2174 (2014).
[9] R. A. Kastelein, W. C. Verboom, N. Jennings, D. de Haan, and S. van der Heul, "The influence of 70 and 120 kHz tonal signals on the behavior of harbor porpoises (Phocoena phocoena) in a floating pen," Mar. Environ. Res. **66**(3), 319–326 (2008).
[10] G. Liu, Z. Yuan, A. Incecik, D. Leng, S. Wang, and Z. Li, "A new biomimetic antifouling method based on water jet for marine structures," Proc. Inst. Mech. Eng., Part M: J. Eng. Marit. Environ. **234**(2), 573–584 (2020).
[11] M. Molitoris, J. Piteľ, A. Hošovský, M. Tóthová, and K. Židek, "A review of research on water jet with slurry injection," Procedia Eng. **149**, 333–339 (2016).
[12] K. Deguchi and A. Walton, "Bifurcation of nonlinear Tollmien-Schlichting waves in a high-speed channel flow," J. Fluid Mech. **843**(12), 53 (2018).
[13] A. S. Jermyn, P. Lesaffre, and C. A. Tout, "Turbulence closure for mixing length theories," Mon. Not. R. Astron. Soc. **476**(1), 646 (2018).
[14] M. H. Hong, S. Y. Cheng, and S. Zhong, "Effect of geometric parameters on synthetic jet: A review," Phys. Fluids **32**, 031301 (2020).
[15] A. Guha, R. M. Barron, and R. Balachandar, "An experimental and numerical study of water jet cleaning process," J. Mater. Process. Technol. **211**(4), 610–618 (2011).
[16] F. Wang, R. Wang, W. Zhou, and G. Chen, "Numerical simulation and experimental verification of the rock damage field under particle water jet impacting," Int. J. Impact Eng. **102**, 169–179 (2017).
[17] C. Y. Lee and D. B. Goldstein, "Two-dimensional synthetic jet simulation," AIAA J. **40**(3), 510–516 (2002).
[18] M. Junkar, B. Jurisevic, M. Fajdiga, and M. Grah, "Finite element analysis of single-particle impact in abrasive water jet machining," Int. J. Impact Eng. **32**(7), 1095–1112 (2006).
[19] P. D. Hunter, A. N. Tyler, and N. J. Willby, "The spatial dynamics of vertical migration by microcystis aeruginosa in a eutrophic shallow lake: A case study using high spatial resolution time-series airborne remote sensing," Limnol. Oceanogr. **53**, 2391–2406 (2008).
[20] S. Bayoudh, A. Othmane, L. Mora, and H. Ben Ouada, "Assessing bacterial adhesion using DLVO and XDLVO theories and the jet impingement technique," Colloids Surf., B **73**, 1–9 (2009).
[21] K. Barak, W. Elad, and H. D. Haustein, "Analytical re-examination of the submerged laminar jet's velocity evolution," Phys. Fluids **30**(6), 063604 (2018).
[22] E. Schuhler, B. Lecordier, J. Yon, G. Godard, and A. Coppalle, "Experimental investigation of a low Reynolds number flame jet impinging flat plates," Int. J. Heat Mass Transfer **156**, 119856 (2020).
[23] G. J. Liu, H. Y. Li, and Z. Z. Qiu, "A comprehensive numerical analysis of cross-flow vortex-induced vibrations for top tension risers under different flows," Phys. Fluids **32**(2), 027102 (2020).
[24] G. J. Liu, H. H. Hao, and T. T. Yang, "Flow field perception of a moving carrier based on an artificial lateral line system," Sensors **20**(5), 1512 (2020).
[25] M. Tropp, F. Brumerčík, J. Šteininger, P. Weis, and A. Glowacz, "Heat distribution in the deep drawing device components working by high temperatures," IOP Conf. Ser.: Mater. Sci. Eng. **393**, 012075 (2018).
[26] E. Bumrungthaichaichan, "A review on numerical consideration for computational fluid dynamics modeling of jet mixing tanks," Korean J. Chem. Eng. **33**(11), 3050–3068 (2016).
[27] P. Hui and X. Z. Chen, "CFD simulations of gas–liquid–solid flow in fluidized bed reactors—A review," Powder Technol. **299**, 235–258 (2016).
[28] P. Marsh, D. Ranmuthugala, I. Penesis, and G. Thomas, "The influence of turbulence model and two and three-dimensional domain selection on the simulated performance characteristics of vertical axis tidal turbines," Renew. Energy. **105**, 106–116 (2017).
[29] S. Varga, J. Soares, R. Lima, and A. C. Oliveira, "On the selection of a turbulence model for the simulation of steam ejectors using CFD," Int. J. Low-Carbon Technol. **12**(3), 233–243 (2017).

[30]J. Zhao, G. Zhang, Y. Xu, R. Wang, W. Zhou, L. Han, and Y. Zhou, "Mechanism and effect of jet parameters on particle waterjet rock breaking," Powder Technol. **313**, 231–244 (2017).
[31]Y. Gao, D. Hong, Y. Cheng, L. Wang, and X. Li, "CFD simulation for up flow jet-loop reactors by use of bi-dispersed bubble model," Chem. Eng. Res. Des. **141**, 66–83 (2019).
[32]P. Aveiro, *Design of Experiments in Production Engineering* (Springer International Publishing, Basel, Switzerland, 2016).
[33]J. Cao, L. Dai, and Y. Wang, "On incompressible oblique impinging jet flows," J. Differ. Equations **265**, 4687 (2018).
[34]F. Ruehle, "Data science applications to string theory," Phys. Rep. **839**, 1 (2019).
[35]J. Li and L. Liu, "A hybrid genetic algorithm based on information entropy and game theory," IEEE Access **8**, 36602 (2020).
[36]C. Ding, L. Chen, and B. Zhong, "Exploration of intelligent computing based on improved hybrid genetic algorithm," Cluster Comput. **22**, 9037 (2018).
[37]C. Lamnatou, A. Moreno, D. Chemisana, F. Reitsma, and F. Clariá, "Ethylene tetrafluoroethylene (ETFE) material: Critical issues and applications with emphasis on buildings," Renewable Sustainable Energy Rev. **82**, 2186–2201 (2018).
[38]J. Hu, W. Chen, B. Zhao, and D. Yang, "Buildings with ETFE foils: A review on material properties, architectural performance and structural behavior," Constr. Build. Mater. **131**, 411–422 (2017).
[39]M. Marin, R. Ellahi, S. Vlase, and M. M. Bhatti, "On the decay of exponential type for the solutions in a dipolar elastic body," J. Taibah Univ. Sci. **14**(1), 534–540 (2020).
[40]M. Marine, S. Vlase, and R. Ellahi, "On the partition of energies for the backward in time problem of thermoelastic materials with a dipolar structure," Symmetry **11**(7), 863 (2019).
[41]Z. H. Zhang and J. N. Gu, "Pressure variation on shallow water bottom caused by moving ship," Shipbuild. China **02**, 11–16 (2002).